AISTech 2019 — Proceedings of the Iron & Steel Technology Conference
6–9 May 2019, Pittsburgh, Pa., USA
DOI 10.1000.377.135

Effect of Bubble Behavior for a Stopper Rod With Multiple Side-Channel Injection on Bubble Size Distributions in Nozzle and Mold During Continuous Casting of Steel

Seong-Mook Cho and Brian G. Thomas

Department of Mechanical Engineering, Colorado School of Mines,
Brown Hall W370-B, 1610 Illinois Street, Golden, Colorado 80401, USA.
Phone: 303-273-3309
E-mail: seongmookcho1@mines.edu (Seong-Mook Cho) and bgthomas@mines.edu (Brian G. Thomas)

Keywords: continuous casting; argon; bubbles; size distributions; breakup; coalescence; accumulation; water model

INTRODUCTION

Argon gas is often injected to prevent nozzle clogging during continuous casting of steel [1]. In addition, it is well known that the argon gas bubbles help to remove non-metallic inclusions in the mold by capturing the inclusions onto the gas bubble outer-surfaces and floating them upward towards the top slag layer [2,3]. However, unoptimized argon gas injection may be detrimental to final steel product quality. Abnormally high gas flow rate compared to the molten steel flow rate can produce annular or slug flow inside the Submerged Entry Nozzle (SEN) [4,5]. This results in asymmetric jet flow [4,5], shallower jet angle [6], and more turbulence [6], causing excessive surface velocity and severe surface level fluctuations in the mold. In addition, very large bubbles float directly upwards to the surface near the SEN, which may cause slag entrainment into the molten steel pool [7,8,9]. Finally, bubbles can be entrapped by the solidifying steel shell, especially if those are smaller than the primary-dendrite arm spacing [10,11] or if deep hooks form in the meniscus [12,13]. This can lead to bubble-related defects, including blisters [5,14], segregation [15], and slivers from the associated inclusions covering the bubble surface [14]. To decrease these bubble-related defects, it is important to better understand bubble behavior and size distributions in the nozzle and mold.

In this work, the behavior and size distributions of bubbles, injected through a stopper rod with multiple downward-inclined channels in its head, are investigated using 1/3-scale water-model measurements, analytical model calculations, and computational model predictions. Bubble formation at the gas channel exits, bubble breakup, coalescence, and accumulation in the nozzle, and bubble size distributions in the nozzle, port, and mold regions are quantified by visualizing the phenomena using a high-speed video camera, measuring the gas pressure and the bubble size distributions, and analyzing those phenomena, including calculations of gas pressure for bubble formation, initial bubble size, bubble terminal descending velocity, residence time, and changes in bubble size distribution due to bubble accumulation. This paper builds on previous work [16] as velocity and turbulence of the fluid flow in the nozzle are calculated with Computational Fluid Dynamics (CFD). Finally, the initial bubble size model validated with the water model measurements, is extrapolated to estimate argon bubble size and bubble frequency in the molten steel caster.

METHODOLOGY

Water Model Experiments

Water-air system experiments were conducted using a 1/3 scale water model to investigate argon bubble behavior and size distributions in the nozzle and mold during continuous steel-slab casting. The model consists of the tundish, stopper rod, SEN, and mold as shown in Figure 1. Vertical movement of the stopper rod controls the water flow rate from the tundish through the SEN into the mold, by changing the size of the annular gap between the stopper-rod head and the bottom of the tundish where it curves into the SEN. Water exits holes in the bottom of the mold into a holding water bath and is pumped continuously back up to the tundish. Dimensions and process conditions for both the real caster and the water model are given in Table I. The casting speed was chosen based on maintaining a constant Froude number. Air is injected through multiple gas channels on the side near the bottom of the stopper rod, as shown in Figure 1(c). Geometric details of the stopper

rod and the gas channels are given in Table II**.** Air flow rate in the water model was chosen to maintain a constant gas volume fraction as follows:

$$\frac{q_W}{Q_W + q_W} = \frac{q_{R(1873K)}}{Q_R + q_{R(1873K)}} = \frac{\lambda q_{R(273K)}}{Q_R + \lambda q_{R(273K)}} \tag{1}$$

where Q_W is water volume flow rate, Q_R is molten-steel volume flow rate, q_W is air volume flow rate at 298 K, $q_{R(1873K)}$ is argon volume flow rate at 1873 K, $q_{R(273K)}$ is argon gas volume flow rate at standard temperature and pressure conditions (1 atm, 273K), and λ is gas expansion factor. Because argon gas injected into the molten steel pool is greatly affected by the high temperature of the molten steel and pressure at the branch channel exit, λ is calculated as follows:

$$\lambda = \frac{q_{R(1873K)}}{q_{R(273K)}} = \frac{\rho_{R(273K)}}{\rho_{R(1873K)}} = \left(\frac{P_{273K}}{P_{1873K}}\right) \times \left(\frac{1873K}{273K}\right) = \left(\frac{P_{273K}}{P_{s,tundish\_level} + \rho_s g\left(H_{tundish} - H_{bc}\right)}\right) \times \left(\frac{1873K}{273K}\right) \tag{2}$$

where, $\rho_{R(273K)}$ is argon gas density at standard conditions (1atm, 273K), $\rho_{R(1873K)}$ is argon gas density at 1873K, P_{273K} is 1 atm, and P_{1873K} is molten steel pressure at the branch gas channel exits. $P_{s,tundish\_level}$ is pressure at the top surface of the tundish (1atm), ρ_s is molten steel density, and $H_{tundish} - H_{bc}$ is hydrostatic pressure head distance from the tundish top surface to the branch-channel exit near the tundish bottom. In this work, λ is 4.1, and fluid properties for both molten steel-argon gas and water-air systems are given in Table III.

Once the water-air flow reached steady state in the stopper rod, nozzle and mold, bubble behaviors in the nozzle (Regions 1-7) and mold (Region 8) were captured using a high-speed video camera at 1200 frames/s. The recorded image snapshots were analyzed using the image-analysis program, Image J [17], to quantify the size distributions of the bubbles in each analysis window (ie. region). In addition, during gas injection, instantaneous gas pressure at the main channel inlet was measured every 0.01 s for 10 s using a pressure gauge with 0.05 kPa pressure resolution and a data logger as shown in Figure 1(b).

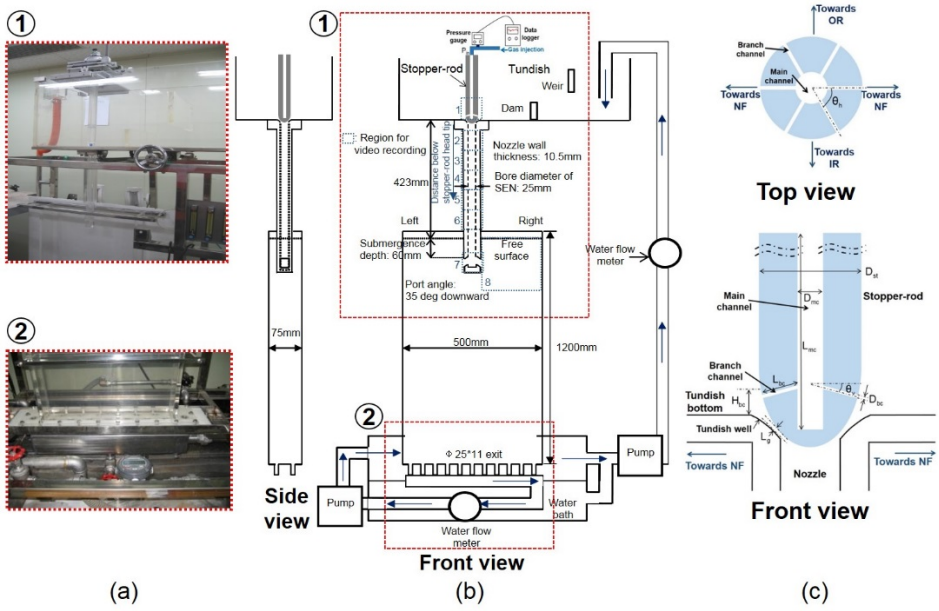

Figure 1. One-third-scale water model showing (a) photos and (b) schematic including region numbers and (c) details of the stopper rod with multi-channels for gas injection.

Table I. Caster dimensions and process conditions

	Real caster (R)	1/3 scale water model (W)
Dimensions		
Nozzle bore diameter: inner / outer	75 / 138 mm	25 / 46 mm
Nozzle bottom well depth	18 mm	6 mm
Nozzle port size: width / height	69.9 / 80.1 mm	23.3 / 26.7 mm
Nozzle port angle	-35° (down) angle	
Tundish level, $H_{tundish}$	1020 mm	340 mm
Distance from nozzle inlet to nozzle port	1449 mm	483 mm
Mold size: thickness / width	225 / 1500 mm	75 / 500 mm
Process conditions		
Steel flow rate	Q_R: 545.6 LPM	Q_W: 35 LPM
Casting speed	$U_{Casting,R}$: 1.61 m/min	$U_{Casting,W}$: 0.93 m/min
Gas flow rate*	Cold (at 273 K): $q_{R\,(273K)}$: **0.8**, 1.5, 2.3, **3.1**, 3.8, 4.6, 5.4, **6.1** SLPM Hot (at 1873 K): $q_{R\,(1873K)}$: **3.1**, 6.2, 9.4,**12.5**, 15.6, 18.7, 21.8, **24.9** LPM	At 298 K: q_W: **0.2**, 0.4, 0.6, **0.8**, 1.0, 1.2, 1.4, **1.6** LPM
Gas volume fraction (hot)*	**0.6**, 1.1, 1.7, **2.2,** 2.8, 3.3, 3.8, **4.4** %	
Submerged depth of nozzle	165 mm	55 mm

* The 3 cases in **bold** were investigated in detail in the nozzle and mold.

Table II. Dimensions of the stopper rod with the gas channels

Dimension	Value
Diameter of stopper rod: D_{st}	42 mm
Diameter of main gas channel: D_{mc}	10 mm
Diameter of branch gas channel: D_{bc}	1 mm
Length of main gas channel: L_{mc}	517.3 mm
Length of branch gas channel: L_{bc}	15.7 mm
Gap size between stopper and tundish well: L_g	2 mm
Vertical-angle of branch channel: θ_v	15° (downward angle)
Horizontal-angle of branch channel: θ_h	60°
Height from tundish bottom to branch channel exit : H_{bc}	10 mm (for water flow rate 35 LPM)

Table III. Comparison of physical properties between molten steel-hot argon and water-air systems

	Molten steel-hot argon system	Water-air system
Liquid density: ρ_l	7000 kg/m^3	998.2 kg/m^3
Gas density: ρ_g	Cold (at 273 K): 1.623 kg/m^3 Hot (at 1873 K): 0.399 kg/m^3	At 298 K: 1.225 kg/m^3
Liquid dynamic viscosity: μ_l	0.007 kg/m·s	0.001 kg/m·s
Gas dynamic viscosity: μ_g	2.1×10^{-5} kg/m·s	1.8×10^{-5} kg/m·s
Interfacial tension coefficient: σ	1.192 N/m	0.073 N/m

Analytical Modeling

Gas pressure for bubble initiation

Video observations show how the initial gas bubbles form at the branch channel exits in the stopper rod. Bubbles form at the branch channel exits in four stages of initiation, expansion, elongation, and detachment stages, as shown in Figure 2. To initiate the bubble formation (Figure 2(a)), gas pressure at the branch channel exit around the liquid pool in the tundish bottom, $P_{bc\text{-}out}$ must overcome the liquid hydrostatic pressure, P_{hyd} and a threshold pressure based on the maximum surface tension force, $\sigma\kappa_{max}$, as given in Eq. (3) following the Young-Laplace equation. Alternatively, $P_{bc\text{-}out}$ can be given by Bernoulli's equation considering the pressure drop from the main channel inlet to the branch channel exit, as follows:

$$P_{bc\text{-}out} = P_{hyd} + \sigma\kappa_{max} = P_{in} + \frac{1}{2}\rho_g\left(u_{mc}{}^2 - u_{bc}{}^2\right) + \rho_g g\left(H_{mc} - H_{bc}\right) - \Delta P_{channels} \quad (3)$$

where P_{in} is inlet gas pressure at the top of the main channel, ρ_g is gas density, u_{mc} is gas velocity in the main channel, u_{bc} is gas velocity in the branch channel, g is acceleration of gravity, H_{mc} is height from the tundish bottom to the main channel inlet, H_{bc} is height from the tundish bottom to the branch channel exit, and $\Delta P_{channels}$ is total pressure drop including three pressure drops: across the main channel (ΔP_{mc}), across a branch channel (ΔP_{bc}) and due to sudden contraction of the cross-sectional area from the main channel to the branch channel (ΔP_{cont}).

Rearranging the above equations gives the minimum pressure at the main channel inlet, P_{in}, that is needed to exceed the threshold pressure at the exit of at least one branch channel and initiate gas bubble formation:

$$P_{in} = P_{hyd} + \sigma\kappa_{max} - \frac{1}{2}\rho_g\left(u_{mc}{}^2 - u_{bc}{}^2\right) - \rho_g g\left(H_{mc} - H_{bc}\right) + \Delta P_{channels} \quad (4)$$

P_{hyd} is calculated as follows:

$$P_{hyd} = \rho_l g\left(H_{tundish} - H_{bc}\right) \quad (5)$$

where ρ_l is liquid density and $H_{tundish}$ is height of the top-surface water level above the tundish bottom.

Surface tension force is maximum with the largest bubble-surface curvature when the hemisphere bubble diameter equals the branch channel diameter.

$$\sigma\kappa_{max} = \frac{2\sigma}{r_{bc}} \quad (6)$$

where σ is surface tension coefficient and r_{bc} is radius of the branch channel exit. $\Delta P_{channels}$ is calculated as follows:

$$\Delta P_{channels} = \Delta P_{mc} + \Delta P_{bc} + \Delta P_{cont} = \frac{128\mu_g}{\pi}\left(\frac{L_{mc}q_{g,mc}}{\left(D_{mc}\right)^4} + \frac{L_{bc}q_{g,bc}}{\left(D_{bc}\right)^4}\right) + \frac{1}{2}\rho_g\left(0.42\left(1 - \frac{\left(D_{bc}\right)^2}{\left(D_{mc}\right)^2}\right)\right)\left(u_{bc}\right)^2 \quad (7)$$

where μ_g is gas dynamic viscosity, D_{mc} is main channel diameter, D_{bc} is branch channel diameter, L_{mc} is main channel length, L_{bc} is branch channel length, $q_{g,mc}$ is total gas volume flow rate in the main channel, and $q_{g,bc}$ is gas volume flow rate in each branch channel ($q_{g,mc}/6$).

Initial bubble size

After initiating bubble formation, the gas bubble starts to protrude from the channel exit, Figure 2(a), and then expands and elongates as shown in Figure 2(b) and (c). Then, the bubble is detached from the stopper-rod wall due to the shearing drag forces of the fast liquid flow through the gap between the nozzle inlet and the stopper-rod head region as shown in Figure 2(d). To calculate this initial bubble size, a two-step semi-analytical model of bubble formation in downstream flow by Bai and Thomas [18] was applied, using the process parameters for the current stopper-rod gas-injection system.

During the expansion stage (model step 1), Figure 2 (b), the bubble sits on the tip of the gas channel exit and is assumed to attain a spherical shape, instantaneously obeying the following force balance including drag force F_d (left term), buoyancy / gravity force F_b (right first term), and surface tension force F_{sur} (right second term),

$$\frac{1}{2}C_d\rho_l\left(\overline{u_l}\right)^2\pi\left(r_{ex}\right)^2 = \frac{4}{3}\pi\left(r_{ex}\right)^3\left(\rho_l - \rho_g\right)g\cos\theta_v + \frac{1}{2}\pi r_{ex}\sigma f_\theta\left(\overline{u_l}\right) \quad (8)$$

where C_d is drag coefficient according to Reynolds number [19], $\overline{u_l}$ is steady average liquid velocity across expanding bubble, r_{ex} is expanded radius of the gas bubble to be solved, θ_v is vertical angle of the branch channel, and f_θ is a contact angle function that depends on the static contact angle and difference between contact angles (advancing contact angle, θ_a and receding contact angle, θ_r) above and below the bubbles [18].

In the elongation stage (model step 2), Figure 2(c), the bubble elongates along the stopper-rod surface when the drag force starts to exceed the surface tension and buoyancy force. Thus, the bubble has an ellipsoid shape at the stopper-rod head surface, due to this shearing effect of the flowing liquid. The equation [18] to predict final bubble size, $d_g\left(=2r_{el,s}\sqrt{e}\right)$ just before it detaches from the stopper-rod head is given as follows:

$$5.2692\frac{\pi U_{tun}}{q_{g,bc}\left(D_{tun}\right)^{1/7}}\int_{r_{ex}}^{r_{el,s}}\left(r^{15/7}\left(ar+b\right)^{3/2}+\frac{ar^{22/7}}{2}\left(ar+b\right)^{1/2}\right)dr=2r_{el,s}\left(e\right)^{3/2}+\frac{D_{bc}}{2}-r_{ex} \tag{9}$$

where $q_{g,bc}$ is average gas volume flow rate into each active branch channel ($q_{g,mc}/n_{act}$), n_{act} is number of activated branch channels, U_{tun} is average liquid velocity near the branch channel exit, D_{tun} is hydraulic diameter in the tundish bottom region, a and b are constants related with r_{ex}, the expansion radius, $r_{el,s}$, the horizontal radius of the elongated bubble to be solved, and e, the elongation factor of the bubble [18].

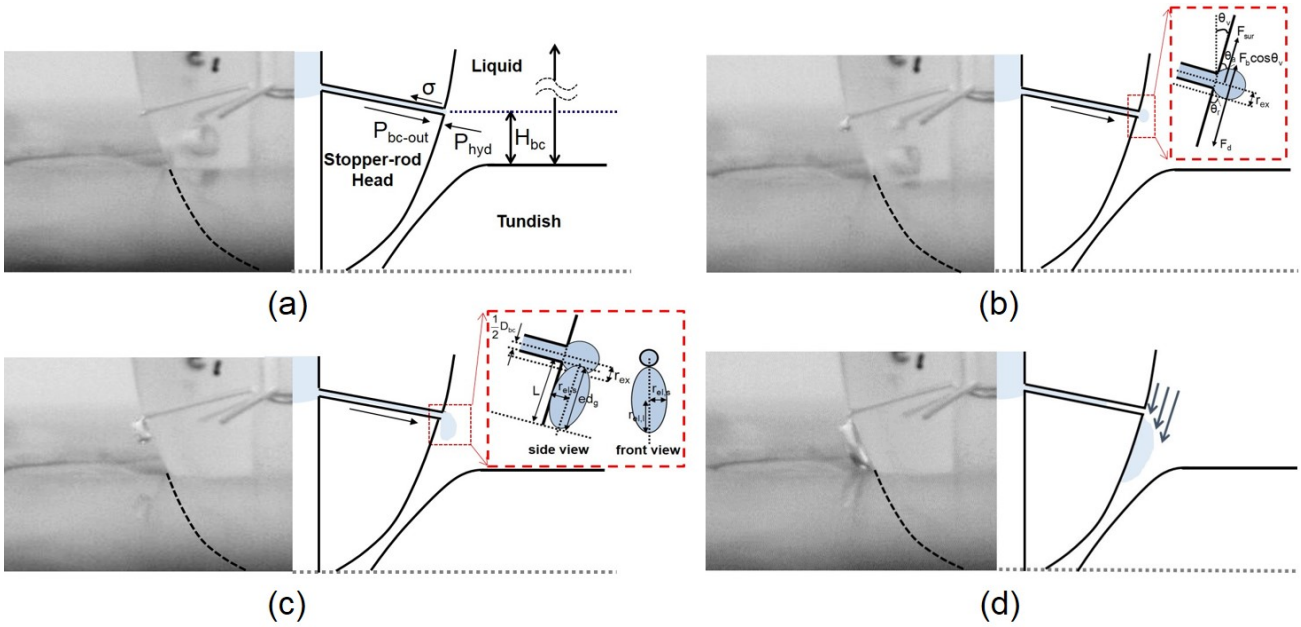

Figure 2. Bubble formation mechanism (left: photo and right: schematic) showing: (a) initiation, (b) expansion, (c) elongation, and (d) detachment.

Bubble terminal descending-velocity

To calculate the residence times of bubbles in the nozzle, the bubble terminal descending-velocity, $u_{g,terminal,\,i}$ is calculated from a force balance between the drag force (left term) and the buoyancy / gravity force (right term) on each gas bubble size as follows:

$$\frac{1}{2}\rho_l\left(u_l-u_{g,terminali}\right)^2C_dA_i=\frac{1}{6}\left(d_{g,i}\right)^3\left(\rho_l-\rho_g\right)g \tag{10}$$

where $d_{g,i}$ is gas bubble diameter i, u_l is liquid velocity in the nozzle, A_i is cross sectional area, which is calculated as $\pi\left(d_{g,i}\right)^2/4$, and C_d is drag coefficient which varies with relative Reynolds number and Weber number for the tap water-air system [20].

Rearranging Eq. (10) gives $u_{g,terminal,\,i}$ as follows:

$$u_{g,terminal,i} = \frac{Q_l}{A_{nozzle}} - \sqrt{\frac{4}{3}\frac{(\rho_l - \rho_g)}{\rho_l}\frac{d_{g,i}}{C_d}g} \tag{11}$$

where Q_l is liquid flow rate in the nozzle and A_{nozzle} is cross-sectional area of the nozzle.

Bubble size distribution based on accumulation

Changes in the bubble size distribution due to gas accumulation in the nozzle were simply estimated based on terminal descending velocity of each bubble size. Inside the nozzle between Regions 3 and 6, the total number of bubbles of each diameter, $n_{3\text{-}6,i}$ was predicted based on the bubble size distribution measured in Region 3, $n_{3,i}$ as follows:

$$n_{3-6,\,i} = n_{3,\,i} f\, t_{residence,\,i} \tag{12}$$

where i is bubble diameter, f is bubble frequency, $t_{residence,i}$ is residence time of a bubble between Regions 3 and 6, calculated as follows:

$$t_{residence,i} = \frac{L_{3-6}}{u_{g,terminal,i}} \tag{13}$$

where $L_{3\text{-}6}$ is vertical distance from Region 3 to 6. From the total number of bubbles of each diameter calculated to reside within Regions 3-6, the number of bubbles in Region 6, $n_{6,i}$ was estimated as follows:

$$n_{6,\,i} = \frac{L_6}{L_{3-6}} n_{3-6,\,i} \tag{14}$$

where L_6 is the vertical height of the analysis window in Region 6. Finally, the population proportion of each bubble diameter in Region 6, $P_{6,i}$ is calculated as follows:

$$P_{6,\,i} = \frac{n_{6,\,i}}{\sum_{i=1}^{n} n_{6,\,i}} \times 100 = \frac{\dfrac{n_{3,\,i}}{u_{g,\,terminal,\,i}}}{\sum_{i=1}^{n} \dfrac{n_{3,\,i}}{u_{g,\,terminal,\,i}}} \times 100 \tag{15}$$

Computational Modeling

A three-dimensional finite-volume CFD model was applied to quantify the fluid flow velocity and turbulence in the stopper-rod nozzle of the 1/3 scale water model. The steady-state Reynolds-Averaged Navier-Stokes (RANS) equations with the standard k-ε model have been solved with a commercial CFD program, ANSYS FLUENT [21] to quantify the time-averaged single-phase (water) turbulent flow in the nozzle. The model used a half domain (adopting 1-fold symmetry) and included the stopper-rod head and nozzle. The domain consists of 0.24-million hexahedral cells. Constant velocity (1.06 m/s) was fixed as the inlet condition at the nozzle inlet which is between the nozzle inner wall and stopper-rod head outer-surface, along with 10^{-5} m^2/s^2 for Turbulent Kinetic Energy (TKE) and 10^{-5} m^2/s^3 for TKE dissipation rate. The velocity was calculated according to the flow rate in the water model and the surface area of the inlet. At the nozzle port, pressure-outlet boundary conditions of ~650 Pa of gauge pressure considering the hydrostatic pressure due to the head of water in the mold, 10^{-5} m^2/s^2 for backflow TKE and 10^{-5} m^2/s^3 for backflow TKE dissipation rate were applied. The inner walls of the nozzle were given by a stationary wall with the no-slip boundary condition. Convergence of solving the equations was defined when all scaled residuals were stably reduced below 10^{-4}.

RESULTS AND DISCUSSIONS

Bubble Formation Mechanism and Initial Size

The number of activated branch channels for bubble formation was measured from the video recordings for various gas flow rates. At lower gas flow rates, all of the branch channels are not activated simultaneously. The number of activated channels generally increases with higher gas flow rate. All six gas-channels are activated when the gas flow rate exceeds a critical value, which is between 1.4 and 1.6 LPM for the conditions in this work. It is likely that slightly non-uniform pressure drops across the branch channels or slightly asymmetric flow near the channel exit in the tundish causes this phenomenon. When the gas flow rate barely exceeds the minimum threshold, only the single branch channel with the largest diameter is able to generate bubbles, which inhibits the system pressure from building up. A significant increase in flow rate is required to increase the system pressure enough to overcome the pressure threshold in the next largest branch channel, and so on.

Gas pressure at the main gas channel inlet was measured for 10 s of steady bubble formation for various gas flow rates [16]. The measured pressure at the main channel inlet are compared with the predicted pressure threshold for bubble formation (calculated using Eqns.4-7) at the same location for several gas flow rates, as shown in Figure 3(a). Both the measurements and the predictions show that higher gas flow rate increases gas pressure at the channel inlet. The predicted pressure threshold increases with flow rate due to the larger pressure drop. The measured average pressure is slightly greater than the predicted pressure threshold as expected, in order to enable flow. The difference generally increases with increasing flow rate, except for jumps when flow through a new branch channel is activated.

After passing through the channels, gas can form bubbles only if the gas pressure can overcome the hydrostatic pressure of the liquid and surface tension force at the branch channel exit. The total bubble frequency increases with increasing gas flow rate, as shown in Figure 3(b). However, as more channels become activated, the frequency per branch channel is always ~100 /s, which means that the formation of one bubble takes ~0.01 s. With increasing gas flow rate, this frequency decreases slightly, which is another cause for the bubble size to increase slightly. Based on the measured total bubble frequency, f, the initial volume-averaged bubble diameter at the branch channel exit, $d_{avg,g}$ can be calculated as follows:

$$d_{avg,g} = \left(\frac{6 q_{g,mc}}{\pi f} \right)^{\frac{1}{3}} \tag{16}$$

These average initial bubble sizes measured in the water model at several gas flow rates are compared in Figure 3(c) with the analytical model predictions of d_g using Eqs. (8) and (9) and with several empirical models suggested by other researchers [22-24]. As shown in Figure 3(c), the empirical models for stagnant liquid flow systems overpredict the initial bubble diameter at the branch channel exit in the stopper rod. This is expected because in the current work, the shearing effect from the high velocity liquid flowing into the gap between the tundish bottom and the stopper rod shortens the time of bubble formation and results in smaller bubbles with higher bubble frequency. In contrast, the two-step analytical model [18] predictions show much better agreement with the measurements. This is because the analytical model was formulated for gas injection into downward flowing liquid, such as encountered in the current flow system. Thus, the analytical model is validated, and can be applied to molten steel-argon gas system in the real plant.

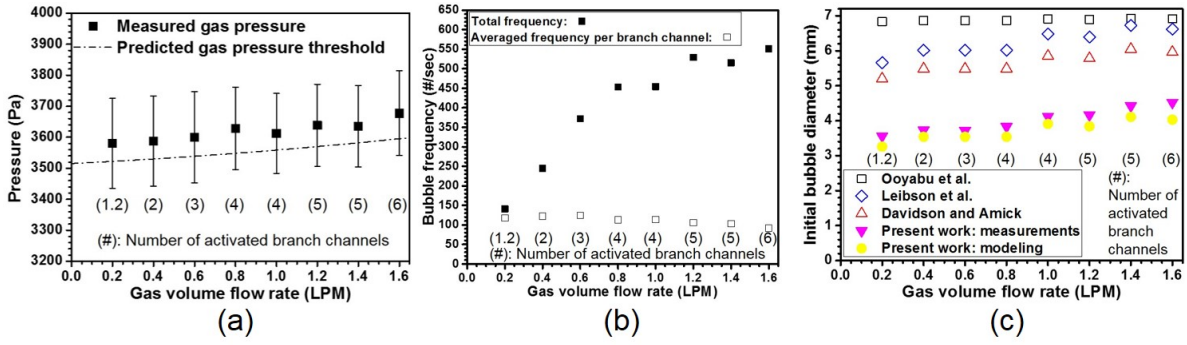

Figure 3. (a) Predicted gas pressure threshold compared with measured gas pressure at the main channel inlet, (b) bubble frequency and (c) initial bubble size at the branch channel exit in the water-air model.

Bubble Breakup, Coalescence, and Accumulation in Nozzle

Bubbles formed at the gas branch-channel exit enter into the highly turbulent flow field in the ~ 2 mm gap between the stopper-rod head and the tundish bottom. As shown in Figure 4(a), bubble size drastically decreases, from an average initial size of ~4.5 mm to <1 mm diameter after passing through the gap into Region 2. The narrow gap forces the bubbles to elongate and the accompanying high velocity gradients produce high shear forces which tear the bubbles apart. In addition, the high turbulent kinetic energy of eddies smaller than the bubble size contributes further to the breakup. Specifically, velocity in the gap exceeds 3 m/s and TKE dissipation rate is ~30 m^2/s^3. This high turbulence allows a stable maximum bubble size of only ~0.7 mm diameter according to the breakup criterion [25]. This is why the bubbles in the SEN are much smaller than the initial bubbles formed at the branch channel exits.

In the nozzle, multiple bubbles are observed to collide and coalesce in complex manners during their flow downward. Some examples of this bubble coalescence behavior are shown in Figure 4(b) for a ~3.4 ms time period. The solid red and dashed blue circles identify two kinds of coalescence phenomena, which are commonly observed in the upper SEN for bubbles smaller than 1.5 mm diameter. The solid red circles show three bubbles touching, causing two of the bubbles to coalesce while the third bubble bounces away. On the other hand, the dashed blue circles show three different bubbles all coalescing into one big bubble. This shows that bubble coalescence is an important mechanism to increase the average bubble size in the nozzle. The big bubbles have lower descending velocity due to higher buoyancy during their downward flow in the nozzle. This also contributes to the bubble size distribution evolving towards larger sizes. After reaching the nozzle well bottom and the ports, the bubbles face high turbulence produced by the jet swirl which shows alternating flow directions [26,27] (clockwise and counter-clockwise directions). Bubbles here experience breakup, as observed in Figure 4(c) near the nozzle bottom. On the other hand, in the upper region of the oversized nozzle ports, where flow is stagnant due to the backflow, bubbles accumulate and coalesce, as observed in Figure 4(c) near the port top.

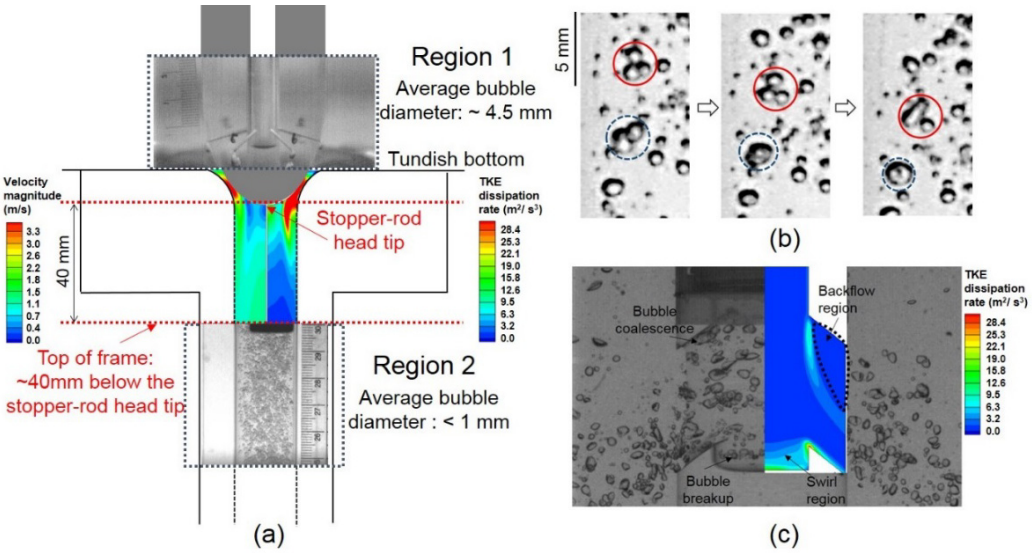

Figure 4. Bubble evolution down the nozzle showing (a) bubble formation (upper), velocity and turbulence near the stopper-rod tip, and resulting breakup into small bubbles (lower), (b) bubble coalescence between Region 3 and Region 4, 150-160 mm below the stopper-rod head tip (1.7 ms between snapshots), and (c) bubble breakup and coalescence in Region 7.

Bubble Size Distributions in Nozzle and Mold

Bubble behavior including formation, breakup, coalescence, and accumulation greatly affects bubble size distributions in the nozzle and mold. Bubbles moving down through four regions in the nozzle (Regions 3-6) were recorded using a high speed video. Example snapshots are shown in Figure 5. To quantify the bubble size distributions in the nozzle and mold, Sauter mean diameter d_{32} is calculated in each analysis window as follows:

$$d_{32} = \frac{\left(d_{avg,V}\right)^3}{\left(d_{avg,A}\right)^2} = \frac{\sum_{i=1}^{n}\left(d_i\right)^3}{\sum_{i=1}^{n}\left(d_i\right)^2} \tag{17}$$

where d_i is measured bubble diameter, and n is the total number of bubbles in the analysis window. This equation uses the volume-average diameter $d_{avg,V} = \sqrt[3]{\frac{6\sum_{i=1}^{n}\frac{\pi}{6}(d_i)^3}{n\pi}}$, and area-average diameter $d_{avg,A} = \sqrt{\frac{\sum_{i=1}^{n}\pi(d_i)^2}{n\pi}}$. In addition, the standard deviation of the Sauter diameter, σ_b is calculated as follows:

$$\sigma_b = \sqrt{\frac{\sum_{i=1}^{n}(d_i - d_{32})^2}{n}} \tag{18}$$

Bubble size distributions in the analysis window of each nozzle region, with air gas flow rates of 0.8 LPM, are given in Figure 5. Going down through the nozzle regions, both average size and standard deviations increase, which agrees qualitatively with previous work in a nozzle below a slide gate [28]. This is due to both bubble coalescence and the accumulation of large bubbles in the descending nozzle flow. Between Regions 3 and 4, the number of bubbles smaller than 1.5 mm decreased greatly (by ~53%), likely due to the coalescence mechanism shown in Figure 4(b). Correspondingly, bubbles larger than 1.5 mm diameter increased in number by 3× between Regions 3 and 4. In Region 6, bubbles larger than 2 mm diameter are slightly more frequent than those in Regions 4 and 5. This suggests that small bubble coalescence occurs mainly between Regions 3 and 4, while larger bubbles gradually accumulate with distance down the nozzle.

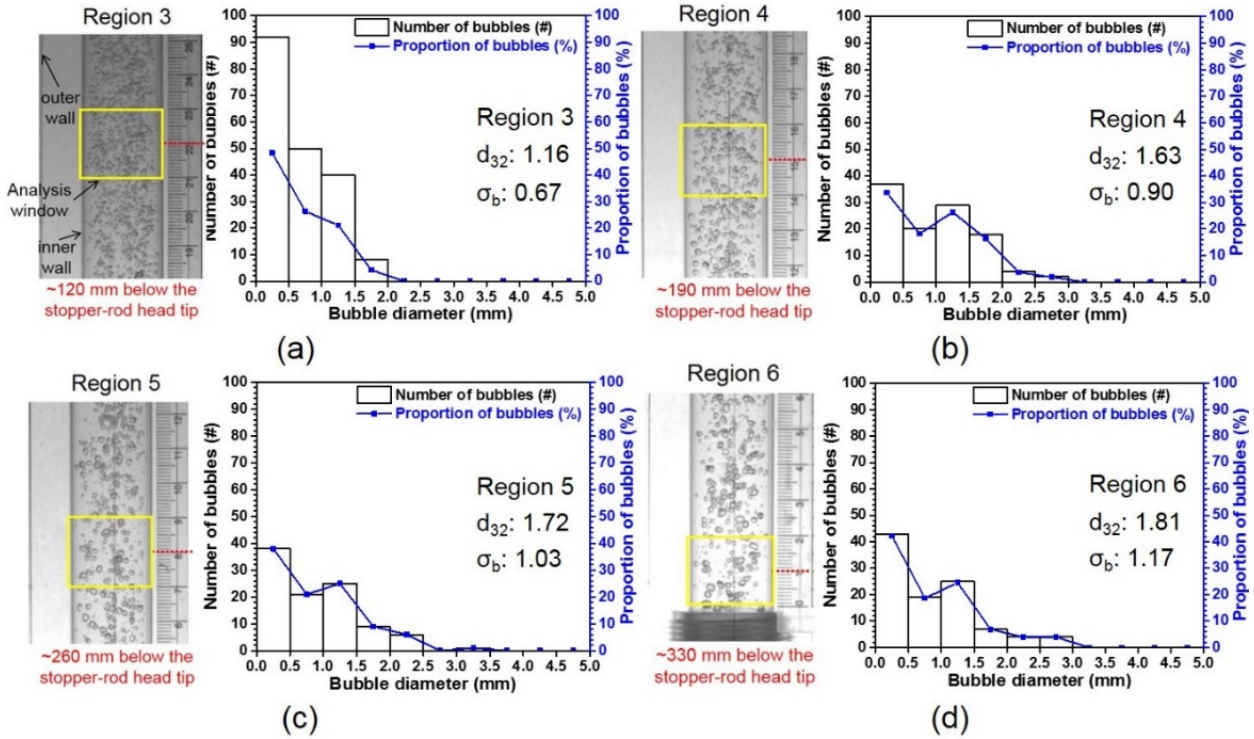

Figure 5. Bubble size distributions in the nozzle with 35.0 LPM (water) and 0.8 LPM (air): (a) Region 3, (b) Region 4, (c) Region 5, and (d) Region 6.

Figure 6(a) shows how terminal descending velocity of bubbles decreases with increasing bubble diameter up to 2.3 mm, as calculated using Eq. (11). Bubbles larger than 2.3 mm diameter have ~0.96 m/s terminal descending velocity, ~20 % lower than the mean liquid flow velocity (~1.2 m/s). Thus, bubbles larger than 2.3 mm diameter have ~ 20% longer residence time in the nozzle than 0.5 mm diameter bubbles. Thus, both the bubble coalescence phenomenon, and the accumulation of larger bubbles due to their longer residence time in the nozzle, are expected to cause the bubble size distribution inside the nozzle to increase with distance down the SEN.

To compare the relative importance of coalescence and accumulation, the change in bubble size distribution between regions 3 and 6 was predicted using Eq. (15), considering only accumulation, and compared with the measurements in Figure 6(b). The predicted proportion of bubbles smaller than 0.5 mm diameter decreases in Region 6, owing to their short residence time. This same trend is observed in the measurements. Correspondingly, bubbles larger than 1 mm accumulate due to their longer residence times, so their proportions increase for both the prediction and measurements. The quantitative discrepancy between the proportion predictions and the measurements is likely due to bubble coalescence inside the nozzle, which appears to be more important than accumulation phenomena.

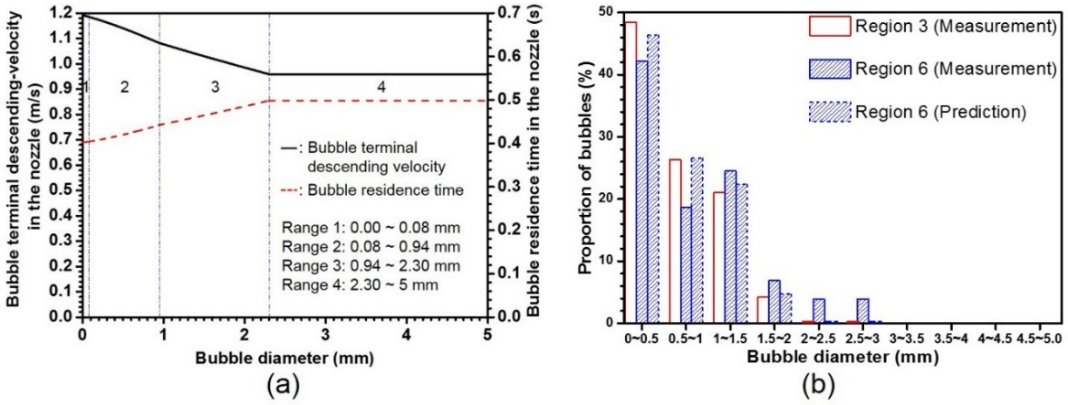

Figure 6. (a) Bubble terminal descending velocity and residence time in the nozzle, and (b) predicted bubble accumulation from Region 3 to Region 6 inside the nozzle and measurements, with 35.0 LPM (water) and 0.8 LPM (air).

In the mold, smaller bubbles typically have longer residence times and accumulate in the mold more than large bubbles, which exit quickly to the top surface [29,30]. Measurements of bubble size distributions were taken in the mold (Region 8), in the yellow rectangular analysis window shown in Figure 7. Larger average and broader size-range (higher standard deviation of bubble size) of bubble size distribution are produced in the mold, as shown in Figure 7. In addition, both average diameter and standard deviation of the bubble size in the mold increase with higher gas flow rate. As the breakup and accumulation mechanisms both tend to decrease the average bubble size in the mold, bubble coalescence in the upper port (Region 7) is clearly the most important mechanism to explain these measured findings.

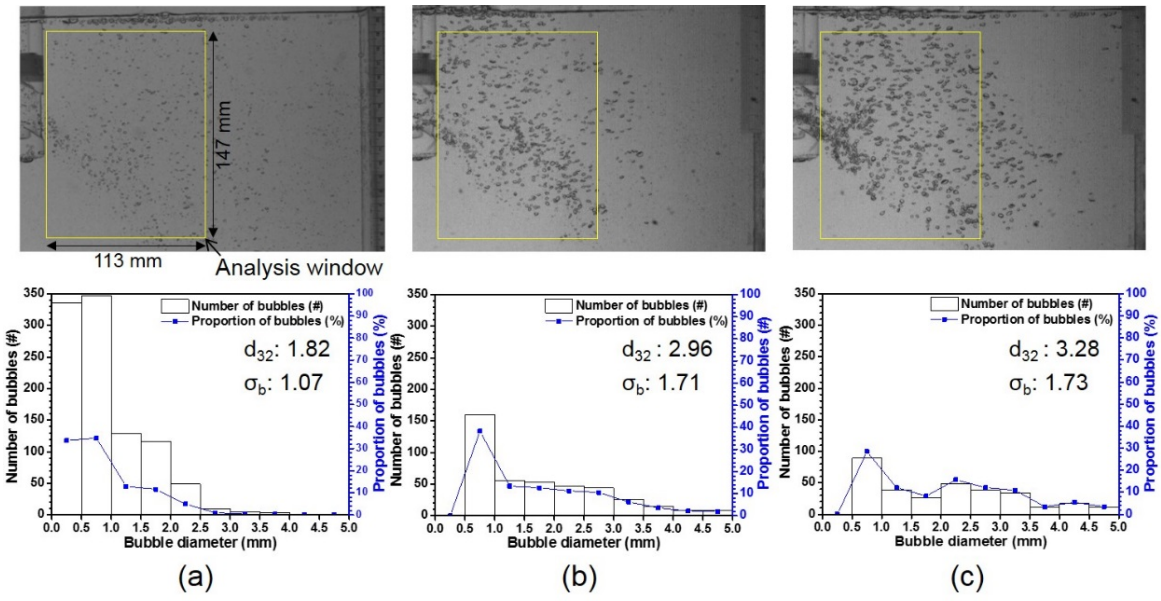

Figure 7. Bubble size distributions in the mold (Region 8) with 35.0 LPM (water) and (a) 0.2 LPM (air), (b) 0.8 LPM (air), and (c) 1.6 LPM (air).

Argon Bubble Size in Molten Steel for Real Caster

The initial bubble size model, validated with the water model measurements in Figure 3(c), was extended to predict the initial size and frequency of argon bubbles in the real steel caster. The steel caster conditions, corresponding to the water model based on Froude similarity and same gas volume fraction, are included in Table I. Figure 8 shows that the predicted initial argon bubble size at the branch channel exit of the real stopper rod, $d_{g,R}$ is 10.5-13.5 mm, which is much larger than the 3-4 mm air-bubble diameter in the water-air system. Increasing the gas flow rate per branch gas channel makes bigger argon bubbles, which matches the trend in the air-water system.

The average volume of the initial argon bubbles in the real caster is ~40× larger than the air bubble volume in the water model. This is partly due to the ~15.6× higher argon gas volume flow rate that is needed to maintain the same gas volume fraction in both systems. In addition, surface tension in molten steel-argon gas system is over 16× higher than water-air system. This likely makes the argon bubble stay on the branch channel exit longer in the steel pool and produces larger bubbles, even though molten steel flow has a larger shearing effect, due to its 1.7× higher velocity near the stopper rod. It is interesting to note, however, that the scaled bubble diameter (dimension) in the steel caster roughly matches the expectation of being 3× bigger, considering the 1/3 scale factor of the water model.

Rearranging Eq. (16) by replacing $q_{g,mc}$ and $d_{avg,g}$ with $\lambda q_{R(273\mathrm{K})}$ and $d_{g,R}$ respectively, gives the total bubble frequency in the real caster, f_R as follows:

$$f_R = \frac{\lambda q_{R(273\mathrm{K})}}{\frac{1}{6}\pi\left(d_{g,R}\right)^3} \tag{19}$$

Compared to the measured total bubble frequency in the 1/3 scale water model (Figure 3(b)), the argon bubble frequency in the real caster should be smaller. This is because the bubble formation time is longer in the molten steel-argon system than in the water-air system and the bubble size is bigger in the real caster.

As investigated from the water-air model measurements, all 3 mechanisms of breakup, coalescence, and accumulation in the nozzle are very significant to determination of the bubble size distributions in the nozzle and mold. Thus, CFD two-phase flow models should include all of these complex bubble phenomena [31,32], if they aim to predict realistic argon bubble size distributions in the nozzle and mold of the real steel caster.

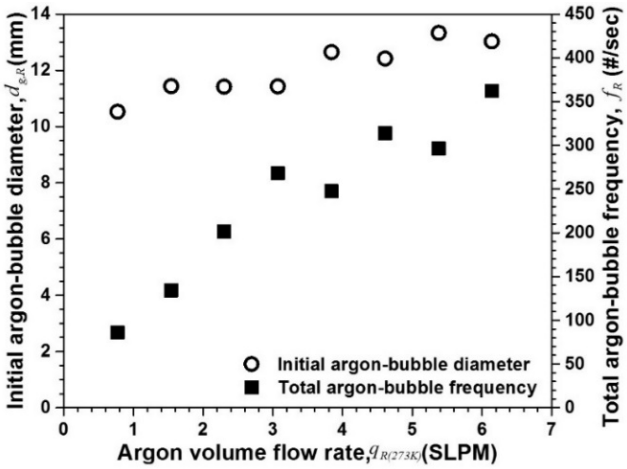

Figure 8. Predicted initial bubble size and bubble frequency of argon gas in the real steel caster.

SUMMARY AND CONCLUSIONS

Bubble behavior and size distributions were investigated in the nozzle and mold of continuous steel-slab casting with a stopper rod having multiple side-channels for gas injection. One-third scale water model experiments using a high-speed video-camera and a pressure gauge, analytical model calculations, and CFD model predictions were applied to quantify bubble formation, breakup, coalescence, and accumulation and their effects on bubble size distributions. The main findings are as follows.

- Gas injected through the multiple channels in this stopper rod forms bubbles in four stages: initiation, expansion, elongation, and detachment.
- Bubble formation is initiated when the inlet gas pressure exceeds the threshold pressure that consists of the pressure drops across the gas channels and due to the sudden area contraction between the gas channels, the hydrostatic pressure from the liquid level in the tundish, and the surface tension force at the branch-channel exit. A higher threshold is needed to produce flow through all 6 branch channels, which are activated in sequence as the gas flow rate is increased.
- With higher gas flow rate, more channels becoming activated decreases the bubble frequency exiting each channel slightly, so the average initial bubble size increases slightly.
- After detaching from the stopper-rod head, bubbles flow into the gap between the stopper-rod head and the nozzle inlet, where they break up due to the high velocity gradients and high turbulence. This drastically decreases bubble size in the region just below the nozzle inlet.
- While flowing down the nozzle, small bubbles coalesce in complex manners while larger bubbles accumulate due to their longer residence time. Both phenomena lead to increasing bubble size with distance down the nozzle, although coalescence is more important.
- In the nozzle well bottom and jet, bubbles breakup due to the high turbulence. In the stagnant upper region of the nozzle port, bubbles coalesce. In the mold, small bubbles accumulate due to their longer residence time. Measured bubble size distributions in the mold are larger and have a broader size range compared with those in the nozzle, suggesting that coalescence is the dominant mechanism for the conditions of this work.
- In both the nozzle and mold regions, the average and standard deviation of the bubble size increases with increasing gas flow rate.
- The semi-analytical model of bubble formation that considers expansion and elongation stages shows good agreement with the measured air-bubble size at stopper-rod branch channel exit in the 1/3 scale water model.
- Applying the validated two-step bubble-formation model to molten steel-argon gas system in the real steel caster predicts much larger (~3×) bubble size and lower bubble frequency, relative to those in the water-air model, as expected considering the 1/3 scale factor.
- The injection of argon gas through multiple branch channels in the sides of the stopper rod tip is expected to be better than central single-channel injection of high gas flow rates through the stopper-rod tip, by producing more stable bubbly flow in the nozzle, avoiding annular / slug flow, and leading to less transient flow variations in the nozzle and mold.

ACKNOWLEDGEMENTS

The authors thank Seon-Hyo Kim and Dae-Woo Yoon, POSTECH for help with the 1/3 scale water model experiments, and Shin-Eon Kang, POSCO Technical Research Laboratories for providing the water model. Support from the Continuous Casting Center at Colorado School of Mines, the Continuous Casting Consortium at University of Illinois at Urbana-Champaign, POSCO, South Korea (Grant No. 4.0002397), and the National Science Foundation GOALI grant (Grant No. CMMI 18-08731) are gratefully acknowledged. Provision of FLUENT licenses through the ANSYS Inc. academic partnership program is also much appreciated.

REFERENCES

1. K. Rackers and B. G. Thomas, "Clogging in Continuous Casting Tundish Nozzles", 78th Steelmaking Conference Proceedings, Nashville, TN, April 2, 1995, Iron and Steel Society, Warrendale, PA, Vol. 78, 1995, pp. 723-734.
2. L. Zhang and B. G. Thomas, “State of the Art in Evaluation and Control of Steel Cleanliness,” ISIJ International, Vol. 43, No. 3, 2003, pp. 271-291.
3. L. Zhang, J. Aoki, and B. G. Thomas, “Inclusion Removal by Bubble Flotation in a Continuous Casting Mold”, Metallurgical and Materials Transactions B, Vol. 37B, No. 3, 2006, pp. 361-379.
4. Zhang, L., S. Yang, X. Wang, K. Cai, J. Li, X. Wan, and B.G. Thomas, “Investigation of Fluid Flow and Steel Cleanliness in the Continuous Casting Strand”, Metallurgical and Materials Transactions B, Vol. 38B, No. 1, 2007, pp. 63-83.
5. M.Burty, C.Pussé, M.Alvarez, P.Gaujé, and G.Grehan, “Fundamental Study of Gas-Liquid Flows in CC Machine”, 84th Steelmaking Conference Proceedings, Baltimore, MD., March 25, 2001, Iron and Steel Society, Warrendale, PA,, Vol. 84 2001, pp. 89-98.

6. H. Bai and B. G. Thomas, “Turbulent Flow of Liquid Steel and Argon Bubbles in Slide-Gate Tundish Nozzles, Part II, Effect of Operation Conditions and Nozzle Design,” Metallurgical and Materials Transactions B, Vol. 32B, No. 2, pp. 269-284, 2001.

7. L.C. Hibbeler and B. G. Thomas, “Mold Slag Entrainment Mechanisms in Continuous Casting Molds”, Iron and Steel Technology, Vol. 10, No. 10, 2013, pp. 121-134.

8. T. Watanabe and M. Iguchi, “Water Model Experiments on the Effect of an Argon Bubble on the Meniscus Near the Immersion Nozzle”, ISIJ International, Vol. 49, No. 2, 2009, pp. 182-188.

9. S. Yamashita and M. Iguchi, “Mechanism of Mold Powder Entrapment Caused by Large Argon Bubble in Continuous Casting Mold”, ISIJ International, Vol. 41, No. 12, 2001, pp. 1529-1531.

10. B. G. Thomas, Q. Yuan, S. Mahmood, R. Liu, and R. Chaudhary, “Transport and Entrapment of Particles in Steel Continuous Casting”, Metallurgical and Materials Transactions B, Vol. 45, No. 1, 2014, pp. 22-35.

11. K. Jin, B. G. Thomas, and X. Ruan, “Modeling and Measurements of Multiphase Flow and Bubble Entrapment in Steel Continuous Casting”, Metallurgical and Materials Transactions B, Vol. 47B, No. 1, 2016, pp. 548-565.

12. J. Sengupta, H.-J. Shin, B. G. Thomas, S.-H. Kim, “Micrograph Evidence of Meniscus Solidification and Sub-Surface Microstructure Evolution in Continuous-Cast Ultra-Low Carbon Steels”, Acta Materialia, Vol. 54, 2006, pp.1165-1173,

13. J. Sengupta, B. G. Thomas, H-J. Shin, G-G. Lee, S.-H. Kim, “A New Mechanism of Hook Formation during Continuous Casting of Ultra-Low-Carbon Steel Slabs”, Metallurgical and Materials Transactions A, Vol. 37A, 2006, pp. 1597-1611.

14. Y. Miki and S. Takeuchi, “Internal Defects of Continuous Casting Slabs Caused by Asymmetric Unbalanced Steel Flow in Mold”, ISIJ International, Vol. 43, No. 10, 2003, pp. 1548-1555.

15. N. Kasai, H. Mizukami, and A. Mutou, “State of Segregation with Bubble in Continuously Cast Slab of Ultra Low Carbon Steel”, Tetsu-to-Hagané, Vol. 89, No. 11, 2003, pp. 1120-1127.

16. S-M. Cho, B. G. Thomas and S-H. Kim, “Bubble Behavior and Size Distributions in Stopper-Rod Nozzle and Mold during Continuous Casting of Steel Slabs”, ISIJ International, Vol. 58, No. 8, 2018, pp. 1443-1452.

17. C. A. Schneider, W. S Rasband, and K. W. Eliceiri, “NIH Image to ImageJ: 25 years of Image Analysis”, Nature Methods, Vol. 9, No. 7, 2012, pp. 671-675.

18. H. Bai and B. G. Thomas, “Bubble Formation during Horizontal Gas Injection into Downward-Flowing Liquid”, Metallurgical and Materials Transactions B, Vol. 32B, No. 6, 2001, pp. 1143-1159.

19. R. Clift, J. R. Grace, and M. E. Weber: Bubbles, Drops, and Particles., Academic Press Inc., 1978, pp. 111-113.

20. J. T. Kuo and G. B. Walis, “Flow of Bubbles through Nozzles”, Int. J. Multiphase Flow, Vol. 14, No. 5, 1988, pp. 547-564.

21. ANSYS FLUENT 14.5-Theory Guide, ANSYS. Inc., Canonsburg, PA, USA, 2012.

22. I. Leibson, E. G. Holcomb, A. G. Cacoso, and J. J. Jamic: “Rate of Flow and Mechanics of Bubble Formation from Single Submerged Orifices”, AIChE J., Vol. 2, 1956, pp. 296-306.

23. L. Davidson and E. H. Amick Jr., “Formation of Gas Bubbles at Horizontal Orifices”, AIChE J., Vol. 2, 1956, pp. 337-342.

24. H. Ooyabu, A. Hiratsuka, R. Tsujino, and M. Iguchi, “Frequency of Bubble Formation from a Multi-Hole Nozzle Attached to a Top Lance”, Mater. Trans., Vol. 50, No. 7, 2009, pp. 1812-1819.

25. G.M. Evans, G.J. Jameson, and B.W. Atkinson, “Prediction of the Bubble Size Generated by a Plunging Liquid Jet Bubble Column”, Chemical Engineering Science. Vol. 47. No. 13/14, 1992, pp. 3265-3272.

26. D.E. Hershey, B.G. Thomas, and F.M. Najjar, “Turbulent Flow through Bifurcated Nozzles”, International Journal for Numerical Methods in Fluids, Vol. 17, No. 1, 1993, pp. 23–47

27. S-M. Cho, B. G. Thomas, H-J. Lee, and S-H. Kim, “Effect of Nozzle Port Angle on Mold Surface Flow in Steel Slab Casting”, Iron and Steel Technology, Vol. 14, 2017, pp. 76-84.

28. N. Kasai and M. Iguchi, “Water-model Experiments on Gas and Liquid Flow in the Continuous Casting Immersion Nozzle”, Tetsu-to-Hagané, Vol. 91, No. 6, 2005, pp. 546-552.

29. K. Jin, S. P. Vanka, and B. G. Thomas, “Large Eddy Simulations of Electromagnetic Braking Effects on Argon Bubble Transport and Capture in a Steel Continuous Casting Mold”, Metallurgical and Materials Transactions B, Vol. 49B, No. 3, 2018, pp.1360-1377.

30. T. Zhang, Z. Luo, H. Zhou, B. Ni, and Z. Zou, “Analysis of Two-Phase Flow and Bubbles Behavior in a Continuous Casting Mold Using a Mathematical Model Considering the Interaction of Bubbles”, ISIJ International, Vol. 56, No. 1, 2016, pp. 116-125.

31. H. Yang, S. P. Vanka, and B. G. Thomas, “A Hybrid Eulerian–Eulerian Discrete-Phase Model of Turbulent Bubbly Flow”, Journal of Fluids Engineering, Vol. 140, 2018, pp. 101202.1-101202.12.

32. H. Yang, S. P. Vanka, and B. G. Thomas, “Modeling Argon Gas Behavior in Continuous Casting of Steel”, Volume 70, No. 10, 2018, pp. 2148–2156.

